IAC–18–C1.5.3

Joint robust structured design of VEGA launcher's rigid-body controller and bending filter

Diego Navarro-Tapia[a]*, Andrés Marcos[a], Samir Bennani[b] and Christophe Roux[c]

[a] *Technology for Aerospace Control (TASC) Lab., Department of Aerospace Engineering, University of Bristol, Bristol BS8 1TR, United Kingdom*; (e-mail: diego.navarro-tapia/andres.marcos@bristol.ac.uk)
[b] *ESA-ESTEC, Noordwijk 2201AZ, The Netherlands*; (e-mail: samir.bennani@esa.int)
[c] *AVIO, VEGA GNC Department, Colleferro 00034, Italy*; (e-mail: christophe.roux@avio.com)
* Corresponding Author

Abstract

This article presents the design of a robust atmospheric control system for the rigid and flexible motion of the VEGA launcher. Unlike the state-of-practice where the design of the rigid-body controller and bending filters are traditionally addressed in a sequential and iterative manner, in this work they are first parametrized following a classical control architecture and then tuned simultaneously using the structured $\mathcal{H}_\infty$ optimization framework. This joint design greatly simplifies the synthesis process and reduces the tuning effort across launch missions. The capabilities of this advanced synthesis framework are exemplified through a design example using the real VEGA 5^{th} flight mission data. The results show that the structured $\mathcal{H}_\infty$ synthesis technique, and proposed methodology, improve the performance and robustness of the launcher, while simplifying the classical current VEGA TVC architecture. This represents a paradigm change in terms of the control design process followed by VEGA, but not in terms of the design objectives and accumulated flight experience heritage by the actual VEGA GNC team.

Keywords: VEGA launcher, robust control synthesis, bending filter design, structured $\mathcal{H}_\infty$

1. Introduction

The atmospheric ascent-flight of a launch vehicle is the most critical phase of the entire launching mission from a control point of view. Based on the measurements from the inertial navigation system (INS), the launch vehicle Thrust Vector Control (TVC) system must compute the necessary engine nozzle deflections to provide stability and follow the guidance commands in the face of parameter dispersion and strong wind gusts.

The design of the atmospheric control system is a complex task that requires the careful consideration of different dynamics such as the elastic deformation of the launch vehicle. The bending modes of the flexible structure can be excited by external perturbations (i.e. noise or wind disturbance) or couplings with the control system. These flexible-body structure interactions may induce instability and must be accounted for in the design stage.

The traditional design state-of-practice consists of several sequential and iterative steps [1]. First, a rigid-body controller is initially designed to stabilise the rigid launch vehicle. Then, the flexible dynamics are added and a set of bending filters is designed to prevent the excitation of the bending modes. Finally, both rigid-body controller and bending filters are manually tuned in an ad-hoc manual integration process until all the system requirements are met.

With respect to the bending filter design, different synthesis approaches can be found in the literature. A constrained numerical optimization was employed for the bending filter design of the NASA Ares-I launch vehicle [2] and also for the attitude hold control system of the International Space Station (ISS) during Orbiter Repair Maneuver operations [3]. In both references, the filters are designed in continuous-time domain and then discretized using a bilinear transformation. In [4], the same numerical optimization is directly applied in the discrete-time domain, while in reference [5] a Recursive Least Squares (RLS) method is used to estimate the most suitable configuration for a discrete notch filter.

Nevertheless, regardless the design approach used, the introduction of the bending filters generally results in degradation of the rigid-body stability margins and performance. This is particularly critical when the frequency of the first structural mode is close to the control system bandwidth.

In this article, unlike the state-of-practice, the rigid-body controller and bending filters are first parameterized and then optimized simultaneously using the structured $\mathcal{H}_\infty$ optimisation approach. This synthesis technique allows to perform the control design for a specified controller structure [6], which is a very suitable feature for the industry. This structured optimisation technique has been widely used in recent years in many applications [7, 8, 9], and more importantly is being considered by industry as a design framework capable of symplifying the launch vehicle control design process [10]. The joint design of the rigid-body controller and the bending filters allows to optimise the rigid-body stability and performance while achieving a proper mode-stabilisation in one single step. Thus, this joint design scheme can significantly simplify the synthesis process and reduce the tuning effort prior to each launcher mission.

The layout of this paper is as follows: Section 2 briefly describes the VEGA launch vehicle, the uncertain vehicle model used for design and the VEGA TVC controller structure. Then in Section 3, the structured $\mathcal{H}_\infty$ optimisation technique is applied to the VEGA launcher to perform a joint design of the rigid-body controller and bending filters. Section 4 analyses the structured $\mathcal{H}_\infty$ design in terms of stability margins and Monte-Carlo simulations. Finally, Section 5 ends with the conclusions.

2. VEGA launcher

2.1 VEGA vehicle and mission

VEGA launcher is the new European Small Launch Vehicle developed under the responsibility of the European Space Agency (ESA) and European Launch Vehicle (ELV/AVIO) as prime contractor. The launcher has successfully performed twelve launches since its maiden flight on 13^{th} February 2012.

VEGA is a single-body launcher, which follows a four stage approach (see Figure 1) formed by three solid propellant motors (P80, Zefiro 23 and Zefiro 9) providing thrust for the first three stages; and, a bi-propellant liquid engine on the 4th stage (AVUM). All stages are controlled using a TVC system. There is also a Roll and Attitude Control System (RACS) performing 3-axes control during the ballistic phase and roll rate control during the propelled phases.

The VEGA launcher is the smallest European launcher with approximately 30 meters high and a diameter of 3 meters. It performs a wide range of missions with single or multiple payloads (from 300 Kg to 2500 Kg) and also different trajectories. These satellites are employed for many specific and Earth observation missions using mainly Sun Synchronous Orbits (SSO) and Low Earth Orbits (LEO).

In this work, all the simulations and designs are applied using the actual VEGA 5^{th} flight mission (VV05) data [11]. The payload of this mission was the Sentinel-2A satellite, part of Europe's Copernicus Earth observation program.

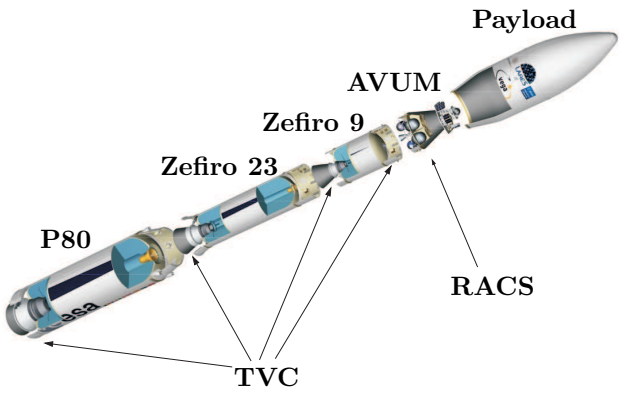

Figure 1: VEGA launcher stage configuration

2.2 Uncertain launch vehicle model

The VEGA launch vehicle model used [12] is obtained using a modelling approach based on the linear fractional transformation (LFT) theory [13]. In particular, the main rigid- and flexible-body dynamics of the launch vehicle are formulated as a LTI state-space representation and then augmented to LFT models by incorporating parametric uncertainties using the MATLAB Robust Control Toolbox [14].

The VEGA launch vehicle can be represented as an upper LFT interconnection, as shown in Figure 2, where $G_{LV}(s)$ represents the nominal plant and also describes how the nominal plant is affected by the uncertainty matrix Δ_{LV}. Note that Δ_{LV} belongs to an uncertainty set $\mathbf{\Delta_{LV}}$ defined by the parametric uncertainties employed for modelling.

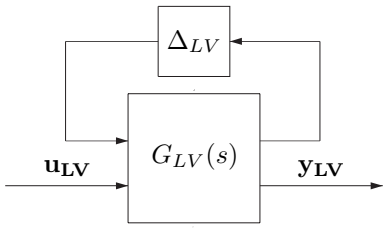

Figure 2: VEGA LFT model

The nominal launch vehicle state-space model is given in equation 1. This model contains the main (rigid and flexible) translational and rotational dynamics of the vehicle. It uses four rigid-body states given by the drift z, yaw attitude angle ψ and their respective derivatives $\left(\mathbf{x_r} = \left[z\ \dot{z}\ \psi\ \dot{\psi}\right]^T\right)$; two flexible-body states accounting for the first bending mode $\left(\mathbf{x_f} = \left[q_1\ \dot{q_1}\right]^T\right)$; three inputs defined by the nozzle deflection angle β_ψ, the acceleration of the actuator $\ddot{\beta}_\psi$ to account for the dynamics of the gimbaled engine (also known as dog-wag-tail effect) and the wind velocity v_w $\left(\mathbf{u_{LV}} = \left[\beta_\psi\ \ \ddot{\beta}_\psi\ \ v_w\right]^T\right)$; and five outputs $\left(\mathbf{y_{LV}} = \left[Q\alpha\ \psi_{INS}\ \dot{\psi}_{INS}\ z_{INS}\ \dot{z}_{INS}\right]^T\right)$, which include the load performance indicator $Q\alpha$ and the measurements at the inertial navigation system (INS) node location for the four rigid-body states.

$$\begin{aligned}\begin{bmatrix}\dot{\mathbf{x_r}}\\ \dot{\mathbf{x_f}}\end{bmatrix} &= \left[\begin{array}{c|c} A_r & A_{rf} \\ \hline A_{fr} & A_f \end{array}\right]\begin{bmatrix}\mathbf{x_r}\\ \mathbf{x_f}\end{bmatrix} + \begin{bmatrix}B_r\\ B_f\end{bmatrix}\mathbf{u_{LV}}\\ \mathbf{y_{LV}} &= \left[\begin{array}{c|c} C_r & C_f \end{array}\right]\begin{bmatrix}\mathbf{x_r}\\ \mathbf{x_f}\end{bmatrix} + D\mathbf{u_{LV}}\end{aligned} \quad (1)$$

As aforementioned, the VEGA LFT model is built by augmenting the nominal LTI model using additive parametric uncertainties. Furthermore, two LFT models are considered to describe the uncertain actuation chain of the VEGA launcher: first, a delay block $G_\tau(s)$ to model all the delays originated by the on-board computers and second, the TVC actuator dynamics $G_{TVC}(s)$, which are described in detail in reference [15]. Both actuation chain LFT models are affected by the uncertainty matrices $\Delta_\tau \in \mathbf{\Delta}_\tau$ and $\Delta_{TVC} \in \mathbf{\Delta_{TVC}}$ respectively. For more details about the LFT modelling approach employed, the reader is referred to reference [16].

2.3 VEGA TVC control architecture

The current VEGA TVC control architecture [17] is described in Figure 3 and can be divided into a rigid-body controller and a set of bending filters. This controller will be referred to as baseline in the rest of the article.

The rigid-body controller is composed of four gains (K_{p_ψ}, K_{d_ψ}, K_z and $K_{\dot{z}}$) and two filters $H_1(s)$ and $H_2(s)$. The gains arise from two proportional derivative (PD) controllers on attitude to provide stabilisation and on drift to limit the lateral speed and position deviations of the vehicle. The filter $H_1(s)$ is added to improve the low-frequency rigid-body stability margins and $H_2(s)$ performs a derivative action to compute the attitude rate error signal $\dot{\psi}_e$. As for the bending filters, $H_3(s)$ notches the first bending mode and attenuates the upper bending modes, and $H_4(s)$ is a low-pass filter to reinforce the attenuation of upper modes on the drift channels.

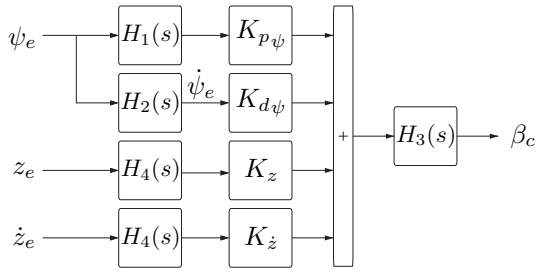

Figure 3: VEGA TVC Control Architecture

The atmospheric-phase TVC controller for the VEGA launcher is defined using 12 linear design sets at approximately every 10 seconds except at lift- and tail-off phases. Then, all the linear controllers are discretized and scheduled versus the non-gravitational velocity.

3. Structured $\mathcal{H}_\infty$ design

This section is dedicated to the joint synthesis of the rigid-body controller and bending filters for the atmospheric phase VEGA launcher. The structured $\mathcal{H}_\infty$ optimisation is performed in continuous-time domain and applied at 9 several flight instants along the atmospheric phase, starting at t=5s and at 8 flight instants between t=20s and t=90s in intervals of 10 seconds.

First, the problem is formulated as a robust control problem and the structured $\mathcal{H}_\infty$ design parametrisation setup is described in detail. Then, the weighting functions used for design are introduced and finally the synthesized rigid-body gains and bending filters are discussed.

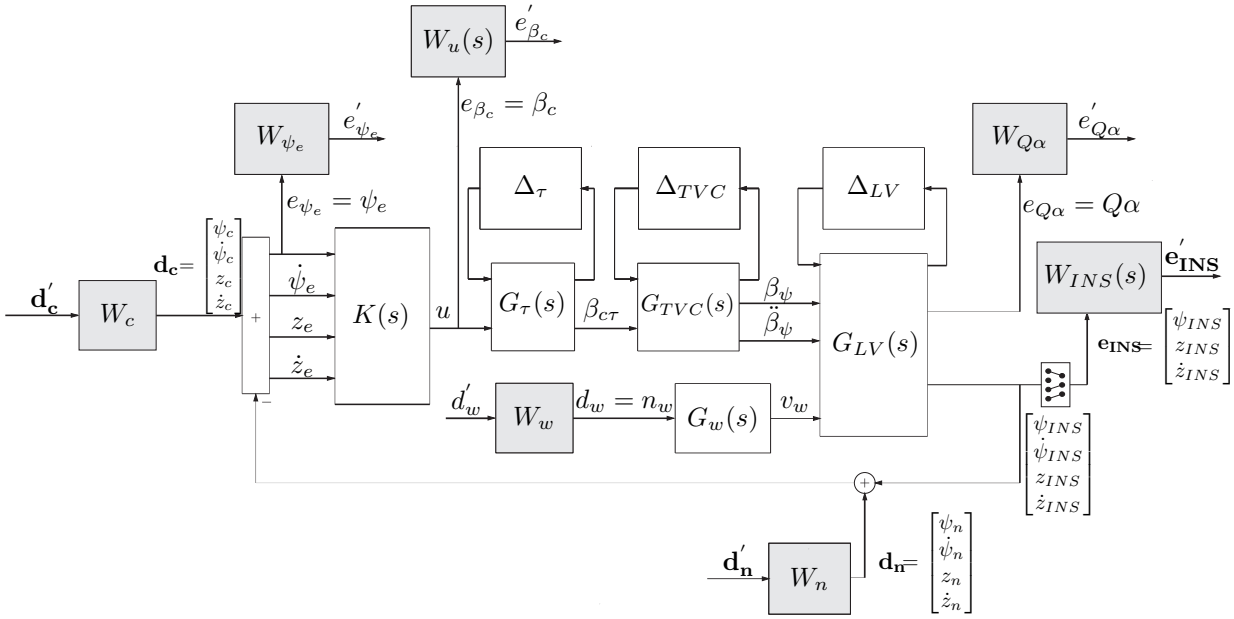

Figure 4: Closed-loop interconnection design

3.1 Problem formulation

The closed-loop system used for design is depicted in Figure 4. This interconnection diagram is composed of the three uncertain LFT models described in Section 2 (i.e. delay, TVC actuator and vehicle model), the controller $K(s)$ and a turbulence wind model $G_w(s)$, which allows to scale the wind channel accounting for statistical severe wind levels (the reader is referred to [15] for further details on this wind model).

The design specifications are imposed via frequency-domain weighting functions (represented by shaded blocks), which are placed at the main inputs and outputs of the design interconnection. The selection of these weighting functions will be discussed in Section 3.3.

The weighted closed-loop system of Figure 4 can be formulated as a robust control problem using the standard $\mathcal{H}_\infty$ interconnection (Figure 5). This representation gathers the main system dynamics, described by the generalised plant $P(s)$, and the design specifications represented by input and output weighting functions (W_{in} and W_{out}).

The inputs of the generalised plant $P(s)$ are formed by the commands, wind disturbance and sensor noise inputs ($\mathbf{d} = \begin{bmatrix}\mathbf{d_c}^T & d_w & \mathbf{d_n}^T\end{bmatrix}^T$), whereas the outputs of $P(s)$ are the main variables to be controlled ($\mathbf{e} = \begin{bmatrix}e_{\psi_e} & \mathbf{e_{INS}} & e_{Q\alpha} & e_{\beta_c}\end{bmatrix}^T$), where e_{ψ_e} is the attitude error signal, $\mathbf{e_{INS}} = \begin{bmatrix}e_{\psi_{INS}} & e_{z_{INS}} & e_{\dot{z}_{INS}}\end{bmatrix}$ represents the (attitude, drift and drift-rate) INS measurements at node location, $e_{Q\alpha}$ is the load performance indicator and e_{β_c} is the commanded actuator deflection.

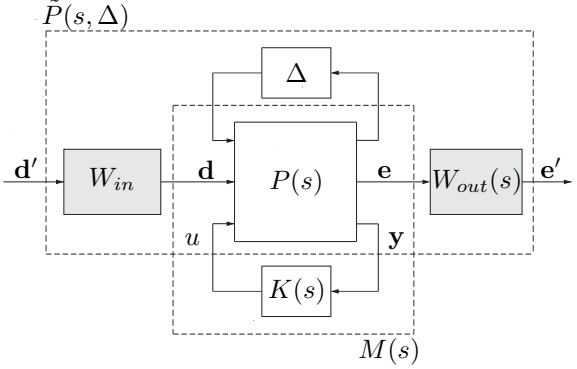

Figure 5: Robust standard $\mathcal{H}_\infty$ interconnection

Note that the tunable controller $K(s)$ is pulled out of the generalised plant $P(s)$, with $u = \beta_c$ representing the controller output and $\mathbf{y} = \begin{bmatrix}\psi_e & \dot{\psi}_e & z_e & \dot{z}_e\end{bmatrix}^T$ the controller input. The structure of $K(s)$ will be described in Section 3.2. In a similar manner, the uncertainty block is also pulled out and represented by $\Delta \in \mathbf{\Delta}$ with $\mathbf{\Delta} = diag(\mathbf{\Delta_{LV}}, \mathbf{\Delta_\tau}, \mathbf{\Delta_{TVC}})$.

The objective of the structured $\mathcal{H}_\infty$ optimisation is to find a stabilizing structured controller $K(s)$ that minimises the $\mathcal{H}_\infty$ norm of the transfer function from the inputs $\mathbf{d}'$ to outputs $\mathbf{e}'$, $\mathcal{T}_{e'd'} = \mathcal{F}_l\big(\tilde{P}(s,\Delta), K(s)\big)$, where $\mathcal{F}_l$ denotes the lower LFT.

3.2 Tunable controller $K(s)$

The TVC structure of the tunable controller $K(s)$ is illustrated in Figure 6. It is composed of a rigid-body controller and a bending filter $H_3(s)$. This structure is based on the actual VEGA TVC control system architecture (see Figure 3) [17], but differs in three main aspects. First, unlike the current design approach, the attitude error rate signal $\dot{\psi}_e$ is assumed available for design. Second, in order to reduce the complexity of the controller structure and to simplify the optimisation process, filters $H_1(s)$ and $H_4(s)$ are not implemented as opposed to the VEGA controller structure. And third, and most importantly, the filter $H_3(s)$ is parametrized in a specific manner (see Section 3.2.2).

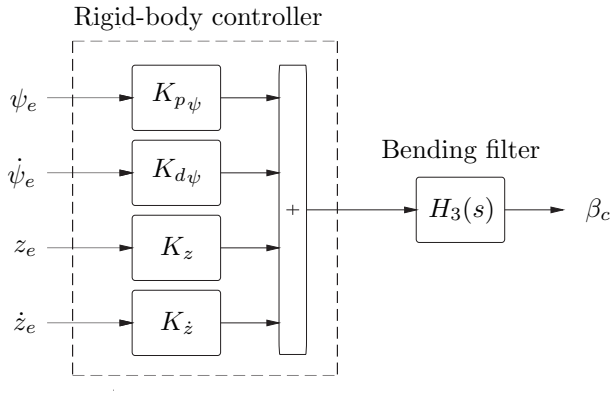

Figure 6: Tunable controller $K(s)$

Next, both tunable rigid-body controller and bending filter are described in detail.

3.2.1 Rigid-body controller

The rigid-body controller retains the baseline four-gains PD controller architecture (K_{p_ψ}, K_{d_ψ}, K_z and $K_{\dot{z}}$).

3.2.2 Bending filter $H_3(s)$

The main objective of $H_3(s)$ is to provide stabilisation against the flexible modes. In particular, the VEGA baseline $H_3(s)$ performs phase stabilisation for the first bending mode (BM) and gain stabilisation for the upper modes. Phase stabilisation consists of shaping the phase of the bending mode so the flexible phase stability margins are guaranteed, whereas gain stabilisation implies a filter design where the bending modes are attenuated to prevent any instability.

Figure 7 shows the frequency response of the VEGA baseline $H_3(s)$ (depicted in thick solid black) at the flight instant t=50s. Note that the values in both x and y axes are not provided for confidentiality reasons. In preparation for the joint design, this baseline filter was analysed and factorized into several filters (see gray dashed-dot lines in Figure 7). It can be seen that using those filters, the baseline filter $H_3(s)$ is roughly retrieved (see thick red dashed line). This factorization was obtained heuristically based on a thorough analysis of the actual shape of the baseline filter. It should be mentioned that the main purpose of this factorization analysis was not to recover exactly the baseline $H_3(s)$ as performed in reference [18] with the rigid-body controller, but to identify a clear modular structure to apply the structured $\mathcal{H}_\infty$ optimisation approach.

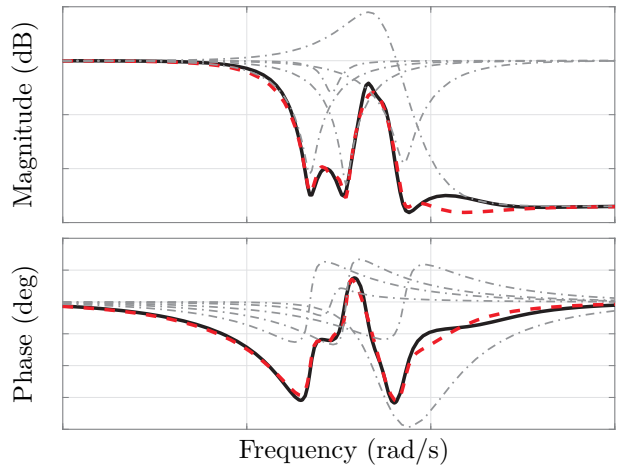

Figure 7: $H_3(s)$ baseline factorization at t=50s

Looking at Figure 7, it is recognized that the baseline bending filter can be factorized into 5 filters (4 notch filters and 1 low-pass filter) as described in equation 2 (shown in the next page for clarity). The first three notch filters attenuate the first bending mode and provide phase stabilisation, whereas the other two filters (notch and low-pass) gain stabilise the upper modes.

$$H_3(s) = \underbrace{\frac{s^2+\eta_1 s+(\underline{\omega_{q_1}}')^2}{s^2+\eta_1/\epsilon_1 s+(\underline{\omega_{q_1}}')^2}}_{\substack{\text{Notch filter 1}\\ [\min 1^{st} BM]}} \underbrace{\frac{s^2+\eta_2 s+(\omega_{q_1})^2}{s^2+\eta_2/\epsilon_2 s+(\omega_{q_1})^2}}_{\substack{\text{Notch filter 2}\\ [\text{nom}1^{st} BM]}} \underbrace{\frac{s^2+\eta_3 s+(\overline{\omega_{q_1}}')^2}{s^2+\eta_3/\epsilon_3 s+(\overline{\omega_{q_1}}')^2}}_{\substack{\text{Notch filter 3}\\ [\max 1^{st} BM]}} \underbrace{\frac{s^2+\eta_4 s+(\underline{\omega_{q_2}}')^2}{s^2+\eta_4/\epsilon_4 s+(\underline{\omega_{q_2}}')^2}}_{\substack{\text{Notch filter 4}\\ [\min 2^{nd} BM]}} \underbrace{\left(\frac{\epsilon_{LP} s^2+\eta_{LP} s+(0.6\omega_{q_2}')^2}{s^2+\eta_{LP} s+(0.6\omega_{q_2}')^2}\right)^3}_{\substack{\text{Low-pass filter}\\ [\text{Upper BMs attenuation}]}} \tag{2}$$

It is worth noting that all filters are parametrized as a function of the frequency values of the first two bending modes (see equation 2). The first and third notch filters are centred at the minimum and maximum expected dispersed frequencies of the first bending mode due to uncertainties ($\underline{\omega_{q_1}}$ and $\overline{\omega_{q_1}}$), whereas the second notch filter is centred at the nominal frequency of the first bending mode (ω_{q_1}). The fourth notch filter is centred at the minimum expected dispersed frequency of the second bending mode due to uncertainties ($\underline{\omega_{q_2}}$), and finally, the fifth filter is a 6^{th}-order low-pass filter which provides attenuation of the upper modes.

Note that all notch filters in equation 2 are parametrized as a function of two parameters: $\eta_\#$ and $\epsilon_\#$ (with $\# = 1...4$), where $\eta_\#$ defines the width of the filter and $\epsilon_\#$ the attenuation at the center frequency of the notch filter. Similarly, the low-pass filter is expressed as a function of ϵ_{LP} (which specifies the attenuation at high frequencies) and η_{LP} (which defines the quality factor of the filter). This parametrization allows having a common structure for the bending filter design along the atmospheric phase and facilitates the subsequent scheduling process.

After the synthesis step, the designed continuous-time bending filter must be converted to the discrete-time domain for its final implementation in the nonlinear, high-fidelity simulator. It is important to remark that this discretization process causes a distortion in the frequency domain, which is very small at low frequencies (below 10 rad/s) but quite significant at high frequencies close to the Nyquist frequency ($\omega_{Nyquist} = \frac{\pi}{T_s}$, with T_s the sampling rate). In particular, due to industrial and heritage reasons, VEGA launcher's sampling rate T_s is too small to capture all the higher modes' dynamics ($\omega_{Nyquist}$ is barely higher than the nominal frequency of the second bending mode). This means that the distortion between the continuous- and discrete-time bending filters will be higher around the second bending mode frequency. Furthermore, this frequency deformation is specially critical when designing notch filters because the central frequency of the filter is shifted and thus, this effect must be taken into account from the design phase.

In order to address this problem, the discretization is performed using Tustin's transformation with the nominal first bending mode frequency as warping frequency ($\omega_p = \omega_{q_1}$). This approach eliminates the scale distortion at ω_p and alleviates the deformation at adjacent frequencies. The selection of ω_{q_1} as warping frequency was taken to specifically preserve the frequency region around the first bending mode, which is critical since it interacts with the rigid-body dynamics.

In addition, all the frequency parameters in equation 2 are also pre-warped to ensure that the notch filters will be centered at the intended frequencies after the discretization process. This Tustin transformation with pre-warping is given by [19]:

$$\omega' = \frac{\omega_p}{\tan(\omega_p T_s/2)} \tan(\omega T_s/2) \tag{3}$$

The $H_3(s)$ design configuration is defined as a function of fixed and tunable parameters for the structured $\mathcal{H}_\infty$ optimisation (see Table 1). The low-pass filter parameters are fixed to provide a certain filter selectivity (or quality factor) and an attenuation of -25 dB to gain stabilise the higher bending modes along the flight envelope. The inclusion of fixed parameters simplifies the optimisation problem and allows to specify a common structure for all the different atmospheric-phase linear designs.

On the other hand, the width of the notch filters ($\eta_\#$) are also fixed whereas the attenuation at the center frequency of the notch filters ($\epsilon_\#$) are defined as tunable parameters. In order to restrict the range of attenuation of the latter, the allowable values of $\epsilon_\#$ are limited in terms of minimum and maximum constraints. Those values have been heuristically selected to define the range covered by the different linear bending filters along the first phase.

Table 1: Structured $\mathcal{H}_\infty$ configuration for tunable bending filter $H_3(s)$

	Fixed parameters		**Tunable parameters**		
Filter	*Parameter*	*Value*	*Parameter*	*min*	*max*
Notch filter 1	η_1	2	ϵ_1	-25 dB	-10 dB
Notch filter 2	η_2	5	ϵ_2	-10 dB	-4 dB
Notch filter 3	η_3	2	ϵ_3	-25 dB	-10 dB
Notch filter 4	η_4	12	ϵ_4	-20 dB	-15 dB
Low-pass filter	η_{LP}	40			
	ϵ_{LP}	-25/3 dB			

Figure 8 defines the allowable frequency responses of the tunable bending filter $H_3(s)$ described by equation 2 and Table 1.

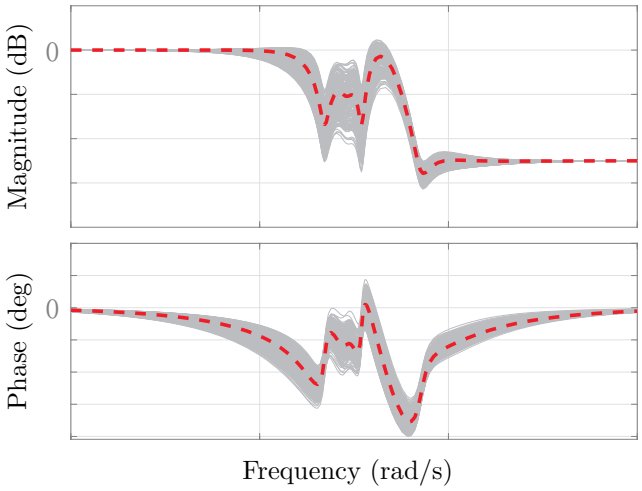

Figure 8: Allowable frequency responses for tunable bending filter $H_3(s)$

3.3 Weighting function selection

In this section, the weighting functions used are described. All the weights related to angles are expressed in degrees; those related to drift and drift-rate in m and m/s; and the output of the Q_α weight is expressed in Pa deg.

Due to the wide dynamic variation of the system during the atmospheric flight, a different set of weighting functions is defined for each of the 9 linear design points. In order to reduce the number of parameters to be tuned and consequently the tuning effort, constant and low order weighting functions are employed.

3.3.1 Input weighting functions

The input weighting functions W_{in} are selected to balance the inputs of the generalised plant $P(s)$ according to their expected variations. W_{in} gathers the weights corresponding to the system commands, wind disturbance input and sensor noise inputs $\big(W_{in} = diag(W_c, W_w, W_n)\big)$.

$W_c = diag(W_{\psi_c}, W_{\dot{\psi}_c}, W_{zc}, W_{\dot{z}c})$ scales the four input commands shown in Figure 4. The range of values taken by W_c is given in equation 4. W_{ψ_c} is fixed to consider a maximum attitude command of 1 deg during the atmospheric phase and $W_{\dot{\psi}}$ is adjusted to balance both attitude channels. Similarly, $W_{\dot{z}c}$ is also fixed to 1 and W_{zc} is tuned to balance both drift channels.

$$W_c = diag\Big(\frac{\pi}{180}, [1-2.6]\frac{\pi}{180}, [5-30], 1\Big) \qquad (4)$$

W_w represents the standard deviation of the white noise input n_w (see Figure 4). This weight is fixed to $W_w = 3$ to consider 99.7% of the wind levels defined by the wind disturbance model $G_w(s)$.

Finally, $W_n = diag(W_{\psi_n}, W_{\dot{\psi}_n}, W_{zn}, W_{\dot{z}n})$ scales the sensor noise inputs according to the expected noise levels from the sensor used by VEGA. The values used for design are described in equation 5:

$$W_n = diag\Big(0.02\frac{\pi}{180}, 0.1\frac{\pi}{180}, 0.01, 0.001\Big) \qquad (5)$$

3.3.2 Output weighting functions

The output weighting functions W_{out} are shaped to specify the control design requirements on the output signals of the generalised plant $P(s)$ $\big(W_{out} = diag(W_{\psi_e}, W_{\psi_{INS}}, W_z, W_{\dot{z}}, W_{Q\alpha}, W_u)\big)$.

In order to achieve a global balanced design two main control modes are employed. A load-relief

control mode is used about the maximum dynamic pressure region (t=40-60s) to minimise the wind disturbance contribution on the structural loads, whereas for the rest of the design points the focus is on minimising the tracking error while keeping low the lateral deviations. These two control modes are mainly accomplished by tuning the drift and drift-rate weights (W_z and $W_{\dot{z}}$), whereas the weighting functions W_{ψ_e}, $W_{\psi_{INS}}$ and $W_{Q\alpha}$ are kept constant for all the design points. This strategy significantly reduces the tuning complexity of each linear design and offers sufficient design flexibility to achieve suitable controllers. Furthermore, the bending filter specifications are implemented through the weight W_u, which is also tuned at each linear design point.

W_{ψ_e} and $W_{\psi_{INS}}$ impose an upper bound on the sensitivity and complementary sensitivity functions of the attitude channel (respectively S_ψ and T_ψ). They are defined as $S_\psi(s) = \mathcal{T}_{\psi_e\psi_c}(s)$ and $T_\psi(s) = \mathcal{T}_{\psi_{INS}\psi_c}(s)$ with $S_\psi(s) + T_\psi(s) = I$. The sensitivity function S_ψ is limited by a constant weighting function of 10 dB (equation 6), while the inverse of $W_{\psi_{INS}}$ is defined as a low-pass filter with a crossover frequency of 10 rad/s to limit the tracking bandwidth, a low-frequency gain of 10 dB to achieve good stability margins and a high-frequency gain of -40 dB to reduce the noise contribution (equation 7).

$$W_{\psi_e} = \frac{180}{\pi}\Big(3.16\Big)^{-1} \quad (6)$$

$$W_{\psi_{INS}}(s) = \frac{180}{\pi}\left(\frac{0.01s+10}{s+\frac{10}{3.16}}\right)^{-1} \quad (7)$$

As previously mentioned, W_z and $W_{\dot{z}}$ are tuned to adjust the control mode at each linear design point. Both weights are defined as constant functions (see equations 8 and 9, where it can be seen the range of values taken by both weights along the atmospheric phase). The load-relief control mode is achieved by setting low values for the inverses of W_z and $W_{\dot{z}}$. This approach directly reduces the wind disturbance effect on the drift-rate channel, and in turn, on the structural load $Q\alpha$ channel which is heavily impacted by the drift-rate contribution. On the other hand, the tracking control mode allows for lateral deviations (using higher values for the inverse of both weights) to reduce the attitude deviations.

$$W_z = \Big([30-500]\Big)^{-1} \quad (8)$$

$$W_{\dot{z}} = \Big([2.5-6]\Big)^{-1} \quad (9)$$

The structural load weighting function $W_{Q\alpha}$ is fixed throughout the atmospheric phase and imposes a maximum angle of attack of 3 deg:

$$W_{Q\alpha} = \frac{180}{\pi}\Big(3Q\Big)^{-1} \quad (10)$$

Finally, the weighting function W_u enforces constraints to avoid actuator saturation and reduce high-frequency actuation. In addition, since W_u is located at the output of the bending filter, this weight is also shaped to achieve the desired frequency response for the bending filter $H_3(s)$. The inverse of W_u is expressed as a function of a low-frequency asymptote l_u and the bending filter $H_3(s)$ factorization (see equation 11). Note that the notch filters' width parameters ($\eta_\#$) are kept fixed as described in Table 1. Thus, only the attenuation parameters ($\epsilon_\#$) are tuned for each linear design, including ϵ_{LP} which is adjusted considering that the high-frequency asymptote of the closed-loop channel $\mathcal{T}_{\beta_c\psi_c}$ equals $K_{p_\psi}\epsilon_{LP}$.

$$W_u(s) = \frac{180}{\pi}\Big(l_u H_3(s)\Big)^{-1} \quad (11)$$

3.4 Structured $\mathcal{H}_\infty$ design

As aforementioned, the structured $\mathcal{H}_\infty$ optimisation is applied at 9 several flight instants along the atmospheric phase. Figure 9 shows the obtained rigid-body gains of the structured $\mathcal{H}_\infty$ design as well as those for the baseline controller. The values in the y-axis are not shown for confidentiality reasons.

Looking at Figure 9, it is observed that the attitude gains of the structured design present the same behaviour with time but with higher gains in the case of K_{p_ψ} and slightly lower gains for $K_{d\psi}$. Furthermore, the structured $\mathcal{H}_\infty$ exhibits higher drift gains K_z, especially about the maximum dynamic pressure favouring the reduction of wind-induced structural loads. Similarly, the drift-rate gains $K_{\dot{z}}$ are also higher along the atmospheric flight for the new design.

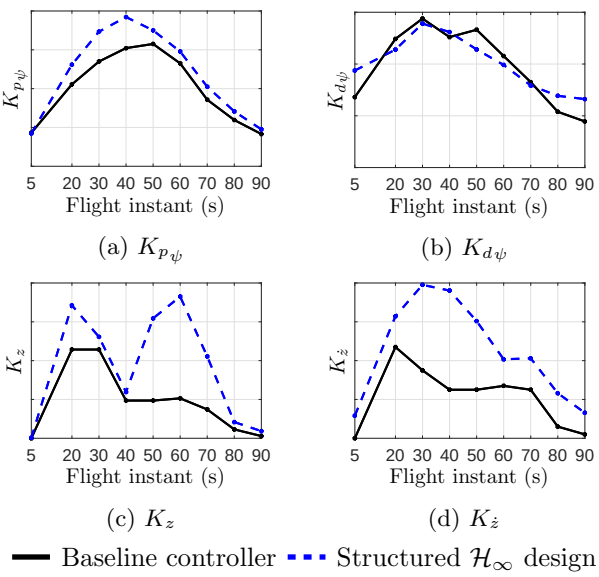

Figure 9: Comparison of rigid-body gains along the atmospheric phase

With respect to the 9 synthesized continuous-time bending filters, their frequency responses are illustrated in Figure 10. It is worth noticing that all the filters present the same structure but with different attenuation levels for the first bending mode and also shifted by the time-evolving bending mode frequencies. Indeed, note that the frequency of the bending modes increases with time. In addition, it can be seen the attenuation provided by all the filters for the upper modes.

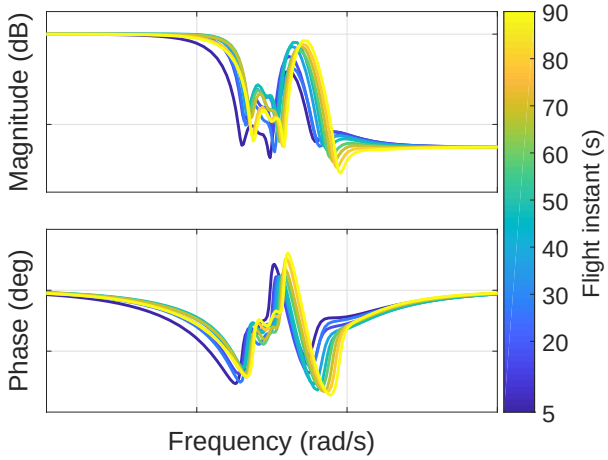

Figure 10: Bode plots of the 9 synthesized bending filter $H_3(s)$ along the atmospheric phase

In order to provide more details about the synthesized bending filters, the frequency responses of the baseline and the structured $\mathcal{H}_\infty$ bending filters at the flight instant t=50s are compared in Figure 11. In this case, the filters are illustrated in the discrete-time domain, which is limited in frequency by the Nyquist frequency.

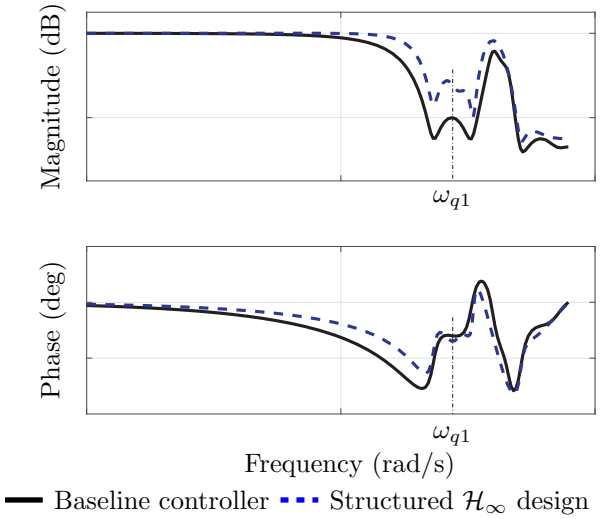

Figure 11: Bode plot of the discrete-time bending filter $H_3(s)$ at t=50s

It is highlighted that the structured $\mathcal{H}_\infty$ bending filter provides a sharper cut-off transition in magnitude and introduces less delay at low frequencies. This strategy significantly reduces the interaction between the first bending mode and the rigid-body dynamics. Indeed, the structured $\mathcal{H}_\infty$ bending filter minimises the degradation of the rigid-body stability margins and improves the decoupling between the rigid-body controller and the bending filter action.

The previous two advantages come at the expense of presenting less attenuation for the first bending mode. Nevertheless, since the first bending mode is phase stabilised, the gain attenuation of this mode is not critical for the design task. Looking at the phase plot, it can be seen that both bending filters add approximately the same phase around the first bending mode frequencies. Furthermore, as it will be shown in Section 4.1, the structured $\mathcal{H}_\infty$ design successfully achieves phase stabilisation providing sufficient margins with respect to the instability points. Finally, it is also observed that the structured $H_3(s)$ filter roughly recovers the roll-off and attenuation level for the upper modes.

4. Simulation results

In this section, the structured $\mathcal{H}_\infty$ controller designed in Section 3 is analysed in terms of linear stability and nonlinear performance.

4.1 Linear stability analysis

The stability of the VEGA TVC controller is traditionally analysed in terms of the classical (gain and phase) stability margins, which are traditionally visualized using Nichols charts (see Figure 12). The margin requirements are defined for each crossing frequency around the critical instability points (indicated in the Nichols chart as red crosses). Note that phase margins (PM) are expressed as the equivalent delay margin (DM) at the frequency ω at which the margin is obtained $\left(DM = \frac{\pi}{180} PM/\omega \text{ with DM in s, PM in deg and } \omega \text{ in rad/s}\right)$.

Three different rigid-body specifications are considered: low-frequency gain margin (LF-GM $\geq$ 0.5 dB), delay margin (DM $\geq$ 40 ms) and high-frequency gain margin (HF-GM $\leq$ -3 dB). In addition, a delay margin ($DM_f \geq$ 20 ms) is defined for phase-stabilized bending modes (i.e. first bending mode), whereas for gain-stabilized bending modes (i.e. upper modes) a gain margin is required ($GM_f \leq$ -3dB).

It is highlighted that all the 9 synthesized linear structured $\mathcal{H}_\infty$ controllers satisfy the above requirements under dispersed conditions. For ease of visualization, only the Nichols chart at the maximum dynamic pressure region (t=50s) is shown in Figure 12. This plot shows that the structured $\mathcal{H}_\infty$ controller presents adequate rigid-body margins. In addition, it phase stabilises the first bending mode and provides enough attenuation to gain stabilise the upper modes.

In addition to the previous classical analysis, the stability of the structured $\mathcal{H}_\infty$ design is also analysed using the structured singular value μ [14], which provides analytically guaranteed bounds on robust stability (RS). In this framework, the system is robustly stable if it is nominally stable and μ is lower than 1 over all frequencies. It should be mentioned that the structured singular value is computed with lower and upper bounds (LB and UB) because the computation of μ is a non-polynominal hard problem.

Figure 13 shows the upper bounds of μ for the structured $\mathcal{H}_\infty$ design at the different linear design points. This plot clearly shows that the RS condition is satisfied at all frequencies. Thus, the system is robustly stable throughout the atmospheric phase.

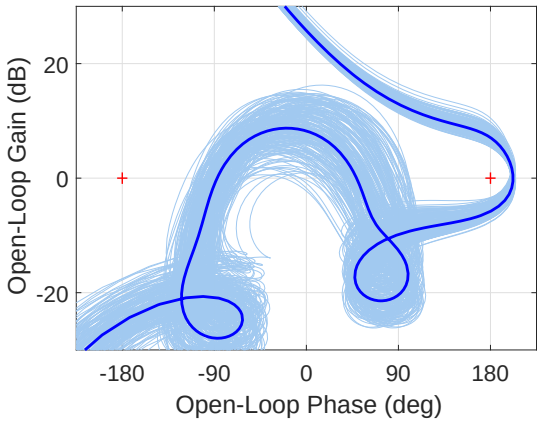

Figure 12: Nichols chart for the structured $\mathcal{H}_\infty$ controller at t=50s (Nominal Dispersed)

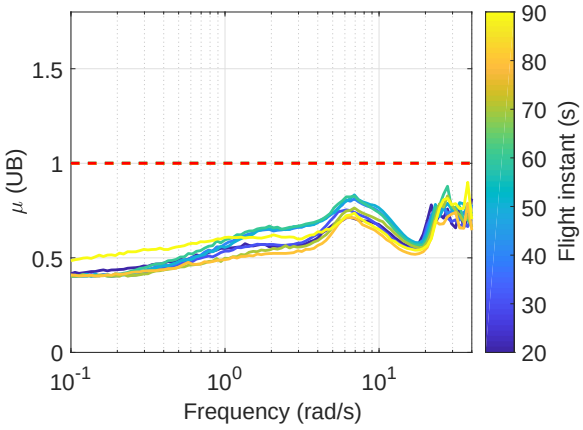

Figure 13: Robust stability analysis (RS bound)

4.2 Nonlinear analysis

Finally, the performance of the synthesized structured $\mathcal{H}_\infty$ controller is evaluated and compared with the baseline controller using *VEGACONTROL*, which is a high-fidelity, nonlinear 6 degrees-of-freedom simulator capturing the atmospheric phase behaviour for the VEGA program.

Before the implementation in the nonlinear simulator, the 9 synthesized linear structured $\mathcal{H}_\infty$ controllers are first discretized as described in Section 3.2.2 (Tustin transformation using the first bending mode frequency as a pre-warping frequency). Then, the individual discrete-domain controllers are gain-scheduled in the same fashion as the actual baseline controller (i.e. using the non-gravitational velocity as scheduling parameter).

The implementation of the baseline controller is as shown in Figure 3. As for the structured $\mathcal{H}_\infty$ controller, the TVC architecture shown in Figure 6 is adjusted for the final implementation to compute the attitude rate error signal $\dot{\psi}_e$ from ψ_e. In this case, instead of using the baseline filter $H_2(s)$, the fixed (non-scheduled) first-order pseudo-derivative filter $H_d(s)$ presented in equation 12 is employed. This configuration further simplifies the tuning effort, since the same filter is used for the whole atmospheric flight, and reduces the controller complexity (1 order versus 4). Note that $H_d(s)$ is also discretized before implementation in the simulator.

$$H_d(s) = \frac{s}{0.02s + 1} \tag{12}$$

Including the filter $H_d(s)$, the final implementation of the structured $\mathcal{H}_\infty$ controller has 15 states, in contrast to the 26 states of the baseline controller.

This nonlinear analysis is based on 4 Monte-Carlo (MC) campaigns of 500 runs (in total 2000 runs). Each MC campaign uses the same parameter scattering but a different wind profile (among them, the estimated wind encountered in VEGA VV05 mission). This MC setup allows to analyse both controllers against different moderate and strong wind gusts at different altitudes.

Figure 14 shows the 2000 nonlinear MC responses of the load performance indicator $Q\alpha$ versus Mach for both controllers. In this case, the load requirement is expressed as a $Q\alpha$ envelope represented in solid red. It is worth noticing that the structured $\mathcal{H}_\infty$ design globally reduces the different $Q\alpha$ peaks throughout the atmospheric flight, particularly around the maximum dynamic pressure region (i.e. Mach 1.25-3).

In addition, other atmospheric performance indicators such as TVC consumption (integrated TVC angle $<$ 250deg) and lateral control requirements (lateral position $<$ 500m and lateral velocity $<$ 15m/s) are analysed in Figure 15. This plot shows the Gaussian distribution of the values of those indicators before the tail-off phase at t=90s, which is the last linear design point for the structured $\mathcal{H}_\infty$ controller.

Looking at Figures 15a-b, it is observed that the TVC actuation performance is improved by the structured $\mathcal{H}_\infty$ design at both lanes, presenting less TVC consumption (mean value) and also less variation. Furthermore, the structured $\mathcal{H}_\infty$ controller provides significantly better (i.e. similar mean but much tighter variations) lateral robust performance in both Y and Z axes as shown in Figures 15c-f. These results give a good statistical insight of the design robustness.

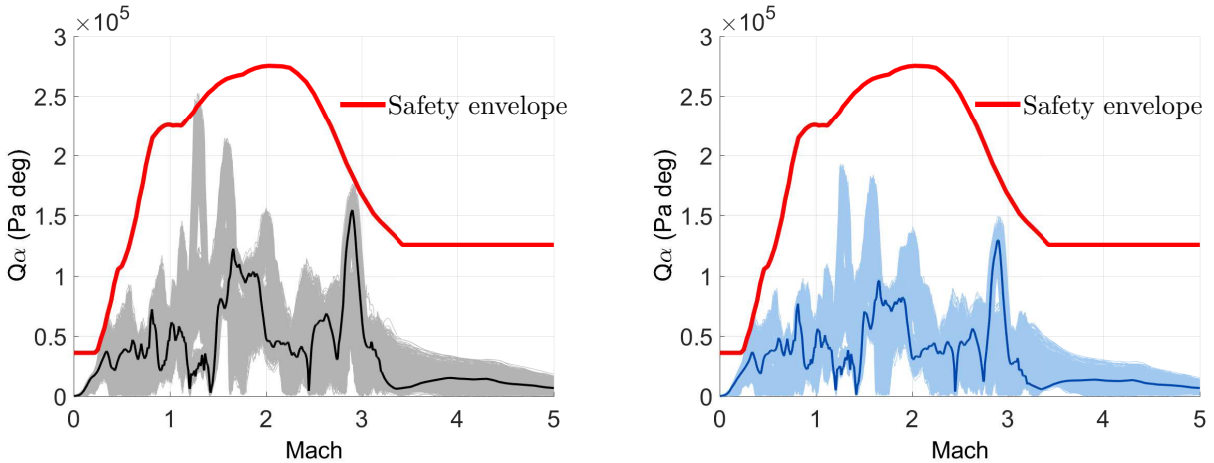

(a) Baseline controller

(b) Structured $\mathcal{H}_\infty$ controller

Figure 14: VEGACONTROL MC $Q\alpha$ analysis

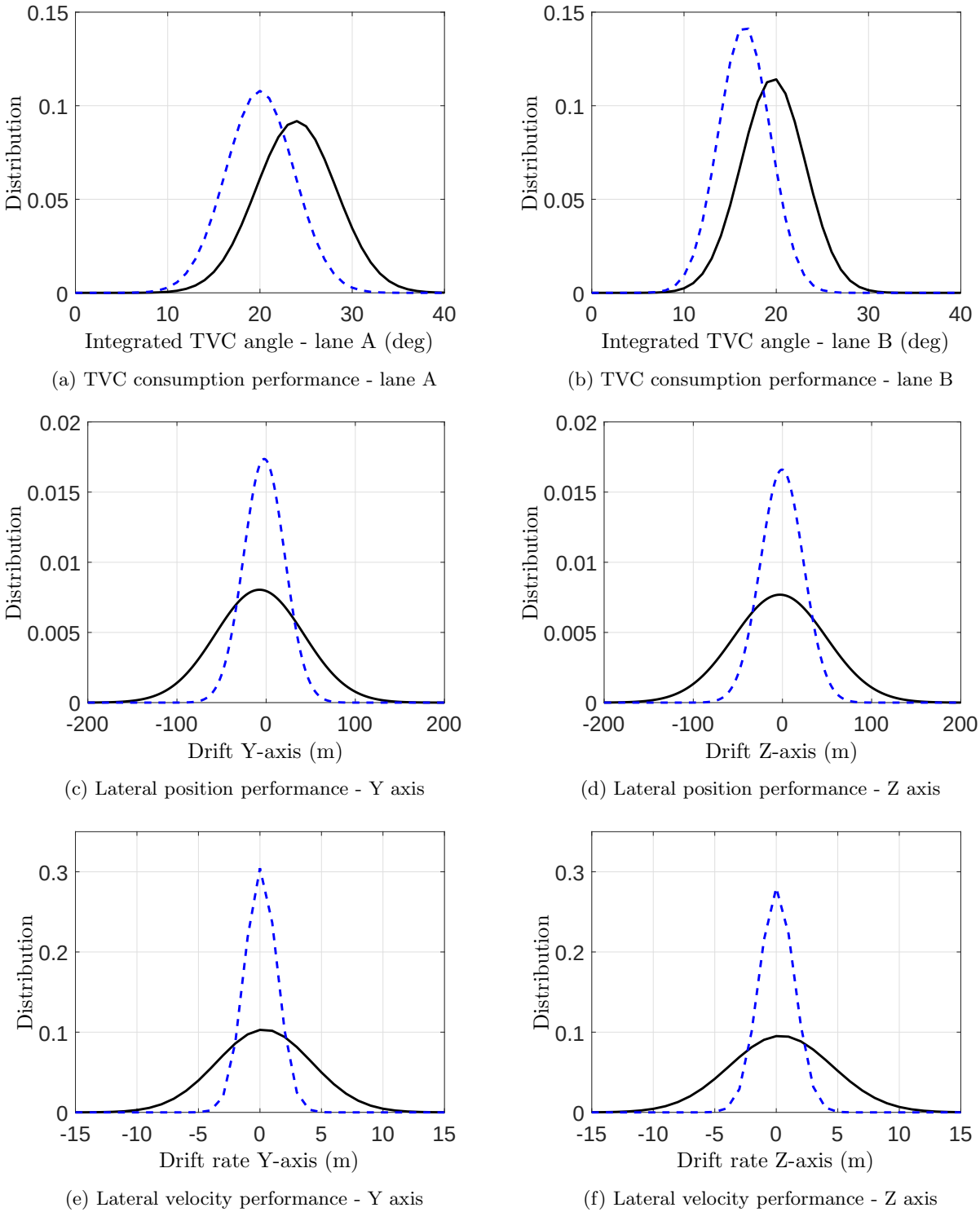

(a) TVC consumption performance - lane A

(b) TVC consumption performance - lane B

(c) Lateral position performance - Y axis

(d) Lateral position performance - Z axis

(e) Lateral velocity performance - Y axis

(f) Lateral velocity performance - Z axis

Figure 15: MC statistical analysis of TVC consumption and lateral control performance

5. Conclusions

This paper presents a joint rigid-flexible controller design of a robust atmospheric control system for the VEGA launcher. The significance of the work is in the augmentation of capabilities of the classical VEGA TVC system via its formulation as a robust control problem framed around the structured $\mathcal{H}_\infty$ optimisation technique.

First, the proposed formulation allows to perform the design of the rigid-body controller and bending filter in one single design procedure. In addition, the proposed framework augments the design capabilities to address well known limitations in launcher control (specifically, wind disturbance and parametric uncertainties). The above augmentation steps are standard in robust control design theory, but they have seldom been integrated and applied in a methodological manner for the control design of a complex nonlinear, high-fidelity launcher system (in the present case the actual VEGA VV05 mission flight).

The results show that the structured $\mathcal{H}_\infty$ synthesis technique, and proposed methodology, improve the performance and robustness of the launcher, while keeping and further simplifying the classical VEGA TVC architecture. This represents a paradigm change in terms of the control design process followed by VEGA but not in terms of the objectives and accumulated flight heritage.

Acknowledgements

This work is funded by the European Space Agency (ESA) through the Networking/Partnering Initiative contract No. 4000114460/15/NL/MH/ats.
Mr. Navarro-Tapia is also the recipient of a Doctoral Training Partnership award No. 1609551 by the UK Engineering and Physical Sciences Research Council (EPSRC).

References

[1] NASA Space Vehicle Design Criteria (Guidance and Control), *Effects of Structural Flexibility on Launch Vehicle Control Systems*. NASA SP-8036, 1970.

[2] J.-W. Jang, R. Hall, N. Bedrossian, and C. Hall, "Ares-I bending filter design using a constrained optimization approach," in *Proceedings of the AIAA Guidance, Navigation and Control Conference and Exhibit*, August 2008.

[3] N. Bedrossian, J.-W. Jang, A. Alaniz, M. Johnson, K. Sebelius, and Y. Mesfin, "International space station US GN&C attitude hold controller design for orbiter repair maneuver," in *Proceedings of the AIAA Guidance, Navigation and Control Conference and Exhibit*, August 2005.

[4] J. S. Orr, *Optimal Recursive Digital Filters for Active Bending Stabilization*. NASA AAS 13-054, 2013.

[5] A. Brito, S. França, and W. L. Filho, "Varying-time notch filter for bending modes active suppression in aerospace systems," in *Proceedings of the* 7^{th} *International ESA-GNC Conference*, 2008.

[6] P. Gahinet and P. Apkarian, "Structured $\mathcal{H}_\infty$ Synthesis in MATLAB," in *Proceedings of the* 18^{th} *World Congress of the International Federation of Automatic Control (IFAC)*, vol. 18, August 2011, pp. 1435–1440.

[7] A. Falcoz, C. Pittet, S. Bennani, A. Guignard, C. Bayart, and B. Frapard, "Systematic design methods of robust and structured controllers for satellites," *CEAS Space Journal*, vol. 7, no. 3, pp. 319–334, 2015.

[8] A. Marcos and M. Sato, "Flight testing of an structured $\mathcal{H}_\infty$ controller: an EU-Japan collaborative experience," in *Proceedings of the* 1^{st} *IEEE Conference on Control Technology and Applications (CCTA)*, August 2017, pp. 1590–1595.

[9] P. Simplício, A. Marcos, E. Joffre, M. Zamaro, and N. Silva, "Synthesis and analysis of robust control compensators for space descent & landing," *Int J Robust Nonlinear Control*, pp. 1–22, 2018.

[10] M. Ganet-Schoeller, J. Desmariaux, and C. Combier, "Structured Control for Future European Launchers," *AerospaceLab Journal*, no. 13, pp. pages 1–10, Nov. 2017.

[11] Arianespace, "VEGA flight VV05," June 2015, http://www.arianespace.com/mission/vega-flight-vv05/.

[12] A. Marcos, S. Bennani, C. Roux, and M. Valli, "LPV modeling and LFT uncertainty identification for robust analysis: application to the VEGA launcher during atmospheric phase," *IFAC-PapersOnLine*, vol. 48, no. 26, pp. 115 – 120, 2015, 1^{st} IFAC Workshop on Linear Parameter Varying Systems LPVS 2015.

[13] J. Doyle, A. Packard, and K. Zhou, "Review of LFTs, LMIs, and mu," in *Proceedings of the 30th IEEE Conference on Decision and Control*. IEEE, 1991.

[14] G. Balas, R. Chiang, A. Packard, and M. Safonov, *Robust Control toolbox*, 2005.

[15] P. Simplício, S. Bennani, A. Marcos, C. Roux, and X. Lefort, "Structured singular-value analysis of the VEGA launcher in atmospheric flight," *Journal of Guidance, Control, and Dynamics*, vol. 39, no. 6, pp. 1342 – 1355, 2016.

[16] D. Navarro-Tapia, A. Marcos, S. Bennani, and C. Roux, "Reconciling full-order LPV design and augmented structured $\mathcal{H}_\infty$ via internal model principle: a launch vehicle application," in *Proceedings of the* 7^{th} *International Conference on Systems and Control (ICSC)*, oct 2018.

[17] C. Roux and I. Cruciani, "Scheduling schemes and control law robustness in atmospheric flight of VEGA," in *Proceedings of the International ESA Conference on Guidance, Navigation and Control Systems*, 2008.

[18] D. Navarro-Tapia, A. Marcos, S. Bennani, and C. Roux, "Structured $\mathcal{H}_\infty$ control design for the VEGA launch vehicle: Recovery of the legacy control behaviour," in *Proceedings of the* 10^{th} *International ESA Conference on Guidance, Navigation and Control Systems (ESA-GNC)*, May 2017.

[19] K. J. Aström and B. Wittemark, *Computer-Controlled Systems: Theory and Design*. Prentice Hall, 2001.